Momentum dependent optical lattice induced by an artificial gauge potential

Chen, Zekai; Yao, Hepeng; Haber, Elisha; Bigelow, Nicholas P.

How to cite

CHEN, Zekai et al. Momentum dependent optical lattice induced by an artificial gauge potential. In: Physical review research, 2022, vol. 4, p. 013124. doi: 10.1103/PhysRevResearch.4.013124

This publication URL: https://archive-ouverte.unige.ch/unige:166544
Publication DOI: 10.1103/PhysRevResearch.4.013124

PHYSICAL REVIEW RESEARCH **4**, 013124 (2022)

Momentum dependent optical lattice induced by an artificial gauge potential

Zekai Chen,[1,2,*] Hepeng Yao,[3] Elisha Haber,[1,2] and Nicholas P. Bigelow[1,2,†]
[1]*Department of Physics and Astronomy, University of Rochester, Rochester, New York 14627, USA*
[2]*Center for Coherence and Quantum Optics, University of Rochester, Rochester, New York 14627, USA*
[3]*Department of Quantum Matter Physics, University of Geneva, 24 Quai Ernest-Ansermet, CH-1211 Geneva, Switzerland*

(Received 7 September 2021; accepted 18 January 2022; published 16 February 2022)

We propose an experimentally feasible method to generate a one-dimensional optical lattice potential in an ultracold Bose gas system that depends on the transverse momentum of the atoms. The optical lattice is induced by the artificial gauge potential generated by a periodically driven multilaser Raman process. We study the many-body Bose-Hubbard model in an effective 1D case and show that the superfluid–Mott-insulator transition can be controlled via tuning the transverse momentum of the atomic gas. Such a feature enables us to control the phase of the quantum gas in the longitudinal direction by changing its transverse motional state. We examine our prediction via a strong-coupling expansion to an effective 1D Bose-Hubbard model and a quantum Monte Carlo calculation and discuss possible applications.

DOI: 10.1103/PhysRevResearch.4.013124

I. INTRODUCTION

In the past two decades, artificial gauge potentials have become a powerful tool for Hamiltonian engineering in cold atom systems. They enable physicists to use the cold atom ensemble for quantum simulation of complicated condensed matter systems, and lead to interesting physics such as creating novel topological defects [1], the spin Hall effect (SHE) [2–5] and spin-orbit coupling (SOC) [6–9]. The SHE in a cold atom ensemble—a phenomenon that arises from a spin-dependent Lorentz-like force acting on moving particles from a transverse direction—has drawn significant attention, as it is closely related to quantum Hall physics and spintronics. To date, much of the work studying the SHE in cold atom systems has focused on weakly interacting single-particle physics such as single-particle spin-dependent trajectories and the SHE induced spin current. On the other hand, SOC—a type of interaction that couples the spin of a particle with its external degree of freedom—is also of extensive interest. It leads to novel energy dispersion [10,11] and topological order [12–15] in both continuous gas and optical lattice systems.

Meanwhile, optical lattices with ultracold atoms are well developed platforms for studying quantum phenomena, especially the many-body effects of condensed matter systems [16]. A familiar aspect of this many-body physics is the superfluid–Mott-insulator (SF-MI) transition, which has been well studied by many groups both theoretically [17,18] and experimentally [18–21]. For optical lattice systems, a natural question arises: what many-body effects involve an artificial gauge potential? A lattice system with a nonzero Peierls phase induced by artificial gauge potentials has been well studied in the weak interaction regime [22–25]. Also, artificial gauge potentials can be used to generate spin-orbit coupling in optical lattices and result in rich phases [26,27]. However, the many-body effects caused by either SOC or the SHE in an optical lattice system with non-negligible interactions demand more exploration. In particular, a system where the lattice potential is determined by the motional state of the atoms is fundamentally different from previous optical lattice systems, and thus is of general interest.

In this paper, we propose to realize a new transverse-momentum-dependent optical lattice (TMDOL) where the longitudinal lattice potential depends on the motional state of the atoms in the transverse dimension. The momentum dependence derives from the same mechanism as the SHE and SOC, which makes it possible to tune the many-body phase of the system via the transverse momentum of the ultracold gas. We create such an artificial gauge potential with translational symmetry in an ultracold pseudospin-$1/2$ gaseous system via a periodically driven Raman process. In previous works studying lattices in momentum space [28–31], the Raman process resulted in a nonzero flux induced by the gauge field, and the momentum took discrete values. By contrast, in the TMDOL considered here, the net flux generated by the artificial gauge field is zero, and the transverse momentum can be tuned continuously. To simplify the problem, we project the Hilbert space to a single spin component and explore the many-body physics of the TMDOL under strong transverse confinement. We construct the effective 1D Bose-Hubbard model and investigate the SF-MI phase diagram using a strong coupling expansion. We then compare our Bose-Hubbard model result to a quantum Monte Carlo (QMC) calculation. Both calculations show that the SF-MI phase transition can

---

[*] zchen57@ur.rochester.edu
[†] nicholas.bigelow@rochester.edu

be induced by changing the average transverse momentum in the TMDOL, which arises as a many-body effect caused by the artificial gauge potential. Specifically, the phase of the quantum gas in the longitudinal direction is determined by the transverse momentum state. In addition, we propose a feasible experimental implementation of the TMDOL and discuss the possible applications.

II. MOMENTUM-DEPENDENT OPTICAL LATTICE IN A PERIODICALLY DRIVEN SPIN-1/2 SYSTEM

Single-particle Hamiltonian formalism

In this section, we describe the theoretical construction of the optical lattice for a pseudospin-1/2 system with a periodically driven Hamiltonian. We start by considering a Hamiltonian for a spin-1/2 system with a periodically driven potential,

$$H = \frac{\vec{p}^2}{2M} + V_{\text{ext}}(\vec{r}) + H_d, \tag{1}$$

where M is the mass of the particle, $V_{\text{ext}}(\vec{r})$ is the spin-independent external trapping potential, and H_d is a periodically driven Hamiltonian,

$$H_d(\vec{r}, t) = \frac{\hbar}{2}\Omega_0 \vec{n}\cdot\vec{\sigma}\cos\omega t, \tag{2}$$

where $\vec{n} = (\cos k_L x \cos k_L z, \cos k_L x \sin k_L z, 0)^T$ is the direction vector, k_L is the wave vector, Ω_0 is the amplitude of the laser field, $\vec{\sigma} = (\hat{\sigma}_1, \hat{\sigma}_2, \hat{\sigma}_3)^T$ is the vector of Pauli matrices, and ω is the frequency of the periodic driving. According to Floquet theory, we can apply a gauge transformation to the Hamiltonian described by the micromotion operator $U = e^{-i\sin\omega t\vec{\Omega}(r)\cdot\vec{\sigma}/2\omega}$ [32–34], where $\vec{\Omega} = \Omega_0\vec{n}$ and the Hamiltonian in the Floquet basis can be written as

$$H_F(\vec{r}, t) = \frac{[\vec{p} - \vec{A}(\vec{r}, t)]^2}{2M} + V_{\text{ext}}(\vec{r}), \tag{3}$$

where $\vec{A}(r, t) = i\hbar U^\dagger \nabla U$ is the non-Abelian gauge potential, with the specific form of the component given in Eqs. (A3) and (A4) in Appendix A [32,33]. We can ignore all terms higher than zeroth order in the Fourier series if the adiabatic condition,

$$\left|\langle\vec{k}|H_F^{(n)}|\vec{k}'\rangle\right| \ll \hbar\omega (n \neq 0), \tag{4}$$

is satisfied, where $H_F^{(n)} = \frac{1}{\mathcal{T}}\int_0^{\mathcal{T}} H_F(t)e^{-in\omega t}dt$ is the nth Fourier component of the Hamiltonian in the Floquet basis, $\mathcal{T} = 2\pi/\omega$, and $|\vec{k}\rangle$ is the momentum state with momentum $\hbar\vec{k}$.

The only term that contributes to the zeroth-order component of the vector potential takes the form

$$A_\xi^{(0)} = \hbar[J_0(a) - 1]\frac{\vec{\Omega}\times\partial_\xi\vec{\Omega}\cdot\vec{\sigma}}{2|\vec{\Omega}|^2}, \tag{5}$$

where $J_0(a)$ is the zeroth-order Bessel function of the first kind, $a = a_0|\cos k_L x|$ with $a_0 = \Omega_0/\omega$ and $\partial_\xi = \partial/\partial\xi$ ($\xi = x, y, z$). We can calculate the specific form of the gauge potential of the zeroth Fourier order by plugging $\vec{\Omega} = \Omega_0\vec{n}$ into Eq. (5) and we get the only nonvanishing component,

$$A_z^{(0)} = \tfrac{1}{2}\hbar k_L[J_0(a) - 1]\sigma_3. \tag{6}$$

The effective Hamiltonian with only zeroth order Fourier terms can be written as

$$H_F^{(0)} = \frac{1}{2M}[\vec{p}^2 - (\vec{A}^{(0)}\cdot\vec{p} + \vec{p}\cdot\vec{A}^{(0)}) + (\vec{A}^2)^{(0)}] + V_{\text{ext}}(\vec{r}), \tag{7}$$

where (see Appendix A)

$$(\vec{A}^2)^{(0)} = \hbar^2 k_L^2\left\{\tfrac{1}{16}a_0^2(1 - \cos 2k_L x) + \tfrac{1}{2}[1 - J_0(a)]\right\} \tag{8}$$

is the zeroth Fourier order component of $\vec{A}^2$. Notice that the zeroth-order effective Hamiltonian in the Floquet basis has discrete translational symmetry with periodicity $a_L = \pi/k_L$, and thus it can be regarded as an optical lattice potential. Putting Eqs. (6)–(8) together, and noticing that the Hamiltonian is proportional to σ_3 with no spin flip terms, which results in a sign difference in the p_z-dependent term for different spin components. Therefore we can project to the spin up subspace to simplify the analysis. Then, we get the effective optical lattice Hamiltonian in the Floquet basis as

$$\begin{aligned} H_L &= \frac{\vec{p}^2}{2M} + \left\{p_z[1 - J_0(a)] + \frac{1}{16}a_0^2[1 - \cos 2k_L x]\right. \\ &\quad \left. + \frac{1}{2}[1 - J_0(a)]\right\}E_r + V_{\text{ext}}(\vec{r}), \end{aligned} \tag{9}$$

where $E_r = \hbar^2 k_L^2/2M$ is the recoil energy. In this work, we only consider the case with $a_0 = 4$ as an example. According to the calculations in Appendix A, the adiabatic condition is always satisfied for the parameters considered here. From Eq. (9), we can see that the lattice potential depends on the transverse momentum, p_z. The nontrivial gauge potential results in a gauge field that exerts a spatially periodic "Lorentz" force on atoms along the x axis due to the motion of atoms along the z axis, which makes the lattice potential p_z-dependent. In addition, the integration of the gauge field calculated from the gauge potential in Eq. (6) over a unit cell is zero, which indicates that the artificial gauge field causes no net flux in the TMDOL system. Such a feature is fundamentally different from the systems in which the artificial gauge potential from the Raman process is used for inducing a Peierls phase in a unit cell [28–31].

We can expand the lattice Hamiltonian in the momentum basis $|\pm 2l\hbar k_L\rangle$ ($l = 0, \pm1, \pm2, \dots$) and diagonalize the Hamiltonian to get the single-particle band structure and eigenstates. In all our calculations, we have used the expansion form of the Bessel function of the first kind $J_q(a) = \sum_{m=0}^{\infty}(-1)^m(a)^{2m+q}/2^{2m+q}\Gamma(m+1)\Gamma(m+q+1)$, where q indicates the order of Bessel function. In practice, we truncate the expansion at the order of $l = \pm 10$, which is sufficiently accurate given our choice of parameters.

Consider the simplest case where $V_{\text{ext}}(\vec{r}) = 0$. When p_z is low the on-site interaction in such a 1D optical lattice will be negligible. In such a weak interaction regime, we can study the physics of the system by solving the single-particle Hamiltonian given by Eq. (9). As shown in Fig. 1, the 1D lattice potential is determined by p_z, which can be experimentally

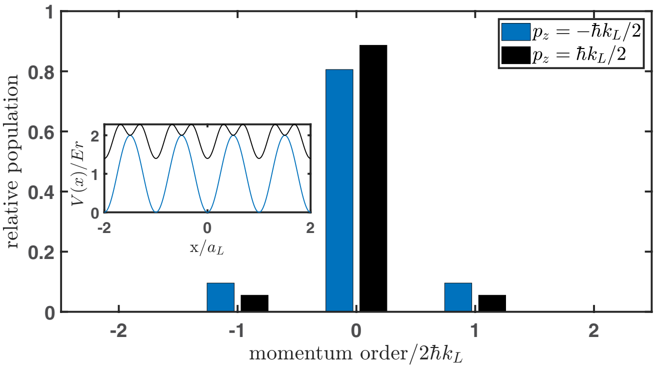

FIG. 1. *s*-band relative population of each momentum state along the x axis with different p_z at zero quasimomentum. The inset plot is the corresponding p_z-dependent 1D optical lattice potential.

observed by measuring the population in each momentum state along the x axis.

III. MANY-BODY PHYSICS IN AN EFFECTIVE 1D SYSTEM

In the previous section, we showed the theoretical formalism of a transverse-momentum dependent optical lattice and discussed the simplest single particle case with negligible interaction between particles. In this section, we explore the many-body physics of the system by considering a non-negligible interaction. Specifically, we introduce a two-dimensional optical lattice confinement along the y and z axes. For simplicity, we further assume the 2D lattice along the y and z axes is deep enough that the tunneling along y and z is negligible. Therefore the system can be regarded as an array of effective 1D Bose gases.

A. Many-body effective 1D Hamiltonian

In the single-particle regime (negligible interaction), all of the atoms will have the same p_z momentum. If the transverse confinement is weak then the spread in p_z momentum will be narrow, but with tight 2D transverse confinement along the y and z axes the ultracold gas will be trapped in an array of effective 1D tubes, and the spreading of the momentum distribution along the z axis will be broad. Throughout this paper, we consider the case where the transverse confinement is strong enough that the tunneling between nearest sites in the y and z is negligible [35,36] (e.g., a lattice depth $V_\perp = 30E_r$). Furthermore, in the following discussions, we consider a homogeneous lattice so that the external harmonic trapping potential along the x axis vanishes for simplicity.

In the effective 1D system, the trapping potential for each site along the y and z axes can be well approximated by a harmonic trap with the characteristic trapping frequency $\omega_\perp = 2\sqrt{V_\perp E_{r,\perp}}/\hbar \gg \mu$, where μ is the chemical potential, and $V_\perp$ and $E_{r,\perp} = \hbar^2 k_\perp/2M$ are the lattice depth and the recoil energy of the 2D lattice. Therefore one can separate the dimensions and the ground-state wave functions along the y and z axes can be well approximated by the harmonic ground-state wave packets,

$$\varphi(y) = (\sqrt{\pi}a_\perp)^{-\frac{1}{2}} e^{-\frac{y^2}{2a_\perp^2}},$$

$$\varphi(z) = (\sqrt{\pi}a_\perp)^{-\frac{1}{2}} e^{-(\frac{z^2}{2a_\perp^2}+i\bar{k}_z z)}, \tag{10}$$

where $a_\perp = \sqrt{\hbar/M\omega_\perp}$ is the characteristic length of the tight harmonic trap and $\bar{k}_z$ corresponds to the average momentum along the z axis, $\langle p_z \rangle = \hbar\bar{k}_z$.

Due to the uncertainty principle, the tight spatial confinement along the transverse directions gives rise to a non-negligible spreading in the momentum space of the atoms along the y and z axes. By integrating along these axes, one gets the single-particle effective 1D Hamiltonian [37]

$$\begin{aligned} H_{\mathrm{1D}}(x, \bar{k}_z) &= \iint dydz\varphi^*(y)\varphi^*(z)H_L\varphi(z)\varphi(y) \\ &= \frac{p_x^2}{2M} + \frac{1}{\mathcal{L}}\int dz \sum_{k_1,k_2} \tilde{\varphi}^*(k_1 - \bar{k}_z)e^{ik_1 z} \\ &\quad \times V(x, p_z)\tilde{\varphi}(k_2 - \bar{k}_z)e^{-ik_2 z} \\ &= \frac{p_x^2}{2M} + \sum_{k_1} |\tilde{\varphi}(k_1 - \bar{k}_z)|^2 V(x, p_z) \\ &= \frac{p_x^2}{2M} + V_{\mathrm{1D}}(x, \bar{k}_z), \end{aligned} \tag{11}$$

where $\mathcal{L}$ is a normalization factor, $V(x, p_z) = \{p_z[1 - J_0(a)] + a_0^2(1 - \cos 2k_L x)/16 + [1 - J_0(a)]/2\}E_r$ and $\tilde{\varphi}(k - \bar{k}_z) = (a_\perp/\sqrt{\pi})^{\frac{1}{2}} e^{-a_\perp^2(k-\bar{k}_z)^2/2}$ is the Fourier transform of $\varphi(z)$ given by Eq. (10). $V_{\mathrm{1D}}(x, \bar{k}_z) = \sum_{k_1} |\tilde{\varphi}(k_1 - \bar{k}_z)|^2 V(x, p_z)$ is the effective 1D potential and can be written as

$$V_{\mathrm{1D}}(x, \bar{k}_z) = \sum_{m=0}^{\infty} V_m(\bar{k}_z)\cos 2mk_L x, \tag{12}$$

where $V_m(\bar{k}_z)$ is the mth-order coefficient that depends on $\bar{k}_z$. We find truncating at $m = 4$ in our calculations works well with our choice of parameters, as the coefficients V_m with $m \geqslant 3$ are much smaller than the leading orders. Notice that we ignored the energy offset, $\hbar\omega_\perp + \hbar^2\bar{k}_z^2/2M$, and used the property $\int dz\exp\{i(k_2 - k_1)z\}/\mathcal{L} = \delta(k_1 - k_2)$.

After writing down the single-particle effective 1D Hamiltonian, we can construct the many-body effective 1D Hamiltonian from the 3D many-body Hamiltonian

$$\begin{aligned} \mathcal{H}_{\mathrm{3D}} &= H_0 + H_{\mathrm{int}}, \\ H_0 &= \int d^3r\hat{\psi}^\dagger(r)H_L\hat{\psi}(r), \\ H_{\mathrm{int}} &= \frac{g}{2}\int d^3r \int d^3r'\hat{\psi}^\dagger(r)\hat{\psi}^\dagger(r')\delta(r - r')\hat{\psi}(r')\hat{\psi}(r), \end{aligned} \tag{13}$$

where the bosonic annihilation operator at jth lattice site is defined as $\hat{\psi}(r) = \sum_j W_j(x)\varphi(y)\varphi(z)\hat{a}_j$ and $g = 4\pi\hbar^2 a_s/M$, where a_s is the s-wave scattering length. $W_j(x)$ and $\hat{a}_j$ is the Wannier function and dimensionless annihilation operator of jth site for the effective 1D Hamiltonian, H_{1D}. We use the Gaussian approximation of the Wannier functions of each site for the lattice potential, $V_{\mathrm{1D}}(x, \bar{k}_z)$, in our calculations. Combining Eq. (11), Eq. (13), and the exact form of $\hat{\psi}(r)$, one

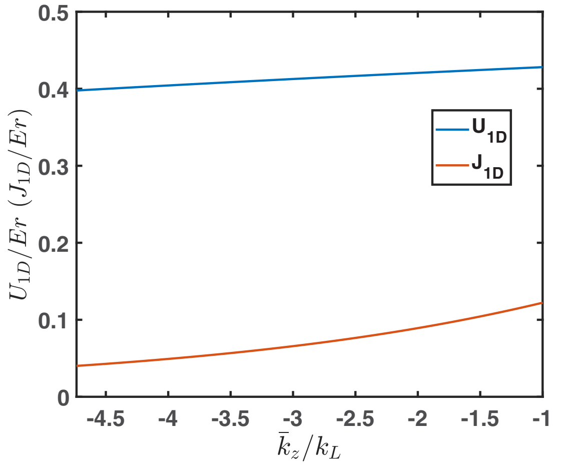

FIG. 2. Effective 1D on-site interaction, U_{1D} (blue line), and effective nearest-neighbor tunneling, J_{1D} (red line), with respect to the average transverse momentum, $\hbar\bar{k}_z$.

gets the effective 1D many-body Hamiltonian of the system:

$$\mathcal{H}_{\mathrm{1D}} = \sum_{i,j}\int dx W_i^*(x)H_{\mathrm{1D}}(x,\bar{k}_z)W_j(x)\hat{a}_i^\dagger\hat{a}_j + \sum_j \frac{g_{\mathrm{1D}}}{2}\int dx|W_j(x)|^4\hat{n}_j(\hat{n}_j-1), \tag{14}$$

where $g_{\mathrm{1D}} = 2\hbar\omega_\perp a_s/(1-Aa_s/a_\perp)$ with $A = 1.036$ [16] and $\hat{n}_j = \hat{a}_j^\dagger\hat{a}_j$ is the number operator of jth site.

B. Bose-Hubbard model and phase diagram

For the effective 1D Hamiltonian, the next-nearest-neighbor tunneling is negligible in a certain regime of $\langle p_z\rangle = \hbar\bar{k}_z$, and the tight-binding approximation is valid. In this regime, we therefore may obtain the effective 1D Bose-Hubbard Hamiltonian,

$$H_{BH} = -\sum_j J_{\mathrm{1D}}(\hat{a}_{j+1}^\dagger\hat{a}_j + \hat{a}_{j+1}\hat{a}_j^\dagger) + \frac{U_{\mathrm{1D}}}{2}\sum_j\hat{n}_j(\hat{n}_j-1) - \sum_j\tilde{\mu}_j\hat{n}_j, \tag{15}$$

where $\tilde{\mu}_j = \mu - \varepsilon_j$. The effective tunneling, J_{1D}, on-site interaction, U_{1D}, and energy offset, ε_j, take the forms

$$\begin{aligned} J_{\mathrm{1D}}(\bar{k}_z) &= -\int dx W_j^*(x)H_{\mathrm{1D}}(x,\bar{k}_z)W_{j+1}(x),\\ U_{\mathrm{1D}}(\bar{k}_z) &= g_{\mathrm{1D}}\int dx|W_j(x)|^4,\\ \varepsilon_j(\bar{k}_z) &= -\int dx W_j^*(x)H_{\mathrm{1D}}(x,\bar{k}_z)W_j(x). \end{aligned} \tag{16}$$

For simplicity, we assume the lattice is isotropic, so that we can drop the site index j so that $\tilde{\mu}_j$ becomes $\tilde{\mu}$.

From the above derivations, we notice that both J_{1D} and U_{1D} depend on the average transverse momentum, $\hbar\bar{k}_z$. In Fig. 2, we show a plot of the effective 1D nearest neighbor tunneling and on-site interaction strength as functions of the average transverse momentum, $\hbar\bar{k}_z$.

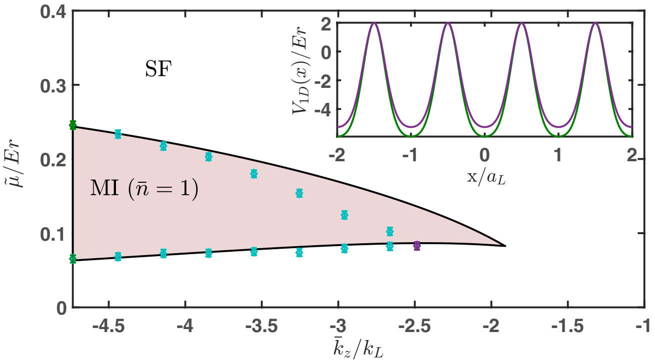

FIG. 3. Phase diagram of the effective 1D TMDOL. The pink shaded area with a black solid line boundary is the $\bar{n} = 1$ Mott lobe calculated from the strong coupling expansion of the effective 1D Bose-Hubbard model. Diamonds with error bars are QMC calculation results with system size $L = 50a_L$ and temperature $k_BT = 0.004E_r$. Note that all error bars are $\pm0.005E_r$. The inset plot shows the corresponding effective 1D lattice potential for $\bar{k}_z = -4.73k_L$ (green line) and $\bar{k}_z = -2.49k_L$ (violet line), which correspond to the potentials for the green diamond and the violet diamond data points, respectively. Blue diamonds with errorbars are QMC results with different transverse momenta.

In a certain regime, the on-site interaction strength is much larger than the nearest-neighbor tunneling so that we can use the strong coupling expansion to calculate the SF-MI phase diagram of the Bose-Hubbard model [38–40]. In the phase diagram, the upper bound, $\tilde{\mu}_p$, and lower bound, $\tilde{\mu}_h$, of the Mott lobe with given occupation $\bar{n}$ and $\tilde{t}(\bar{k}_z) = J_{\mathrm{1D}}(\bar{k}_z)/U_{\mathrm{1D}}(\bar{k}_z)$ are given by $\tilde{\mu}_p = f_p[\bar{n},\tilde{t}(\bar{k}_z)]$ and $\tilde{\mu}_h = f_h[\bar{n},\tilde{t}(\bar{k}_z)]$, where $f_p[\bar{n},\tilde{t}(\bar{k}_z)]$ and $f_h[\bar{n},\tilde{t}(\bar{k}_z)]$ are polynomials obtained from a perturbative calculation in the strong interaction limit. Specifically, in our work, we use Eqs. (B1) and (B2) in Ref. [40] to calculate $\tilde{\mu}_p$ and $\tilde{\mu}_h$. The $\langle p_z\rangle$ dependence of the parameter $J_{\mathrm{1D}}/U_{\mathrm{1D}}$ results in a $\langle p_z\rangle$-dependent phase diagram. The $\bar{n} = 1$ Mott lobe is visible in the phase diagram shown in Fig. 3. The phase diagram displays the tunability of the SF-MI phase transition on the transverse average momentum $\langle p_z\rangle$ in our lattice system. The detailed parameters we use in the calculation are chosen for ^{87}Rb atoms. Specifically, $k_L = 2\pi/\lambda_R$, $\lambda_R \approx 791$ nm $= 2a_L$, $k_\perp = 2\pi/\lambda_\perp$, and $\lambda_\perp = 852$ nm is the wavelength for the 2D optical lattice along the y and z axes.

C. Quantum Monte Carlo calculation

From the above discussion, we know qualitatively that we are expecting a SF-MI phase transition by changing $\langle p_z\rangle$ in the effective 1D system. In this section, we apply a QMC method to find the phase transition.

Here, we use path-integral Monte Carlo calculations in continuous space in the grand-canonical ensemble [41]. We consider the effective 1D many-body Hamiltonian in the continuous space,

$$H_{\mathrm{QMC}} = \sum_{1\leqslant j\leqslant N}\left[-\frac{\hbar^2}{2m}\frac{\partial^2}{\partial x_j^2} + V_{\mathrm{1D}}(x_j,\bar{k}_z)\right] + g_{\mathrm{1D}}\sum_{j<\ell}\delta(x_j - x_\ell), \tag{17}$$

where $V_{1D}(x, \bar{k}_z)$ is the effective potential with the form of Eq. (12). For a given temperature, T, chemical potential, μ, and external potential, $V_{1D}(x, \bar{k}_z)$, we can generate the imaginary-time Feynman diagram configurations with a certain probability distribution. In the following QMC calculations, we use the lowest frequency lattice period, $a_L = \pi/k_L$, and the corresponded recoil energy, $E_r = \hbar^2 k_L^2/2M$, as the space and energy units, respectively. Then, the particle density, $\bar{n} = N/L$, is obtained from the statistics of the closed worldlines, where N denotes the atom number in the ensemble and L the system size. Thanks to the worm algorithm implementations [42,43], we can further compute the superfluid density, ρ_s, efficiently. These two quantities help us to distinguish the MI from the SF phase. We use the same QMC algorithm as in Refs. [18,44–46], where details of the implementations are discussed.

In the actual QMC calculations, we take large enough size, $L = 50a_L$, and small enough temperature, $k_B T = 0.004E_r$, to make sure that our system is in the thermodynamic and zero-temperature limits. We confirm that there is no further finite-size and finite-temperature effects at larger sizes and smaller temperatures. Our final QMC results are shown in Fig. 3 as the blue diamonds with errorbars, which indicate the SF-MI transition boundaries for the corresponding parameters. The transition points to the MI phase are determined by the condition $\rho_s = 0$. At these points, we also find that the particle density, $\bar{n}$, reaches an integer value with zero variation.

We generally find good agreement between the strong coupling expansion from the effective 1D Bose-Hubbard model in Eq. (15) and the QMC calculation from the Hamiltonian in Eq. (17) with many-body interactions for the $\bar{n} = 1$ Mott lobe. Despite the small difference for small $|\bar{k}_z|$, the QMC calculation confirms a significant Mott lobe for $\bar{n} = 1$, which verifies that there exists a transverse-momentum-dependent SF-MI transition. As $\bar{k}_z$ gets closer to zero, the strong coupling expansion and the QMC results start to deviate from each other. As shown by the inset plot of Fig. 3, the lattice potential becomes shallower when $|\bar{k}_z|$ decreases. This leads to the increase of J_{1D}/U_{1D}, and the next-nearest neighbor tunneling starts to become non-negligible. Therefore the Bose-Hubbard model becomes less accurate as $|\bar{k}_z|$ approaches zero and we see the slight disagreement between the two methods. Moreover, the Mott lobe for $\bar{n} = 2$ is shown in Appendix C. We believe the more significant deviation between the results of the two methods is due to the density-dependent ground state [47–49]. This feature also arises in regular optical lattices, and thus we believe that it is not caused by the TMDOL. Despite the slight differences, generally the transverse-momentum-dependent SF-MI transition is still confirmed by both approaches, which displays a many-body effect caused by the artificial gauge potential in our system.

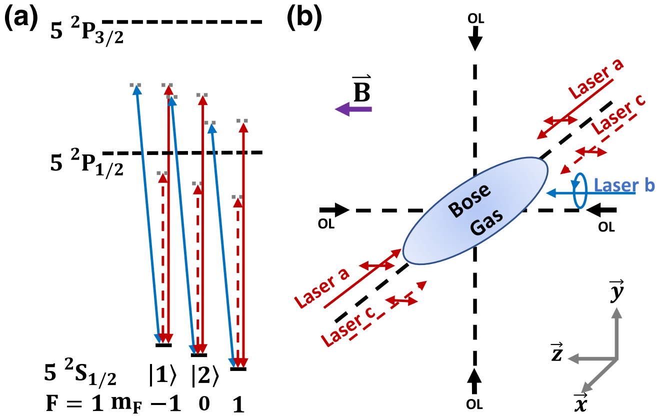

FIG. 4. (a) Level diagram of the Raman process that we consider. Red solid, blue solid and red dashed arrows indicate lasers *a*, *b*, and *c*, respectively. (b) Laser configuration of the Raman process. The laser colors are the same as (a), with their polarizations indicated by the small arrows. The bias magnetic field is in the $+z$ direction, and the four black arrows represent the two-dimensional trapping lattice beams in y-z plane.

IV. A FEASIBLE EXPERIMENTAL IMPLEMENTATION

A. Creation of the periodically driven Hamiltonian

Our goal is to create the periodically driven Hamiltonian in Eq. (2). In this work, we focus on using the atom-laser interaction to construct the periodically driven Hamiltonian. In the following discussions, we consider the dipole interaction of ^{87}Rb atoms with continuous weak (CW) laser fields [50]. More specifically, the pseudospin-1/2 system we consider is formed by two Zeeman states in the $5S_{\frac{1}{2}}, F = 1$ ground state manifold, namely, $|\uparrow\rangle = |F = 1, m_F = -1\rangle$, and $|\downarrow\rangle = |F = 1, m_F = 0\rangle$. In the presence of a bias magnetic field, $\vec{B}$, which defines the z axis of the system, the degeneracy between the two states is lifted. Both states are coupled via a Raman process by applying CW Raman lasers a, b and c, where a is a standing wave along the x axis with π polarization, b propagates in the $+z$ direction with σ^- polarization and c is another standing wave along the x axis with π polarization. The Raman lasers are detuned far enough from the D_1 and D_2 transitions to avoid any excitations over the timescale of the experiment. The states we considered in our calculations and the laser configurations are shown in Fig. 4. Laser coupling to all other states will be negligible.

The periodically driven Raman coupling Hamiltonian can be achieved by modulating the intensity of the Raman lasers a and c by $|\cos\omega t|$, and at the same time modulating the relative phase, η, between lasers a and b such that $\eta(t) = \pi[1 - \mathrm{sgn}(\cos\omega t)]$, where sgn(·) denotes the signum function. Periodic driving of several hundreds of kilohertz can be achieved using an electro-optic modulator (EOM). The electric field of the Raman lasers takes the form

$$\begin{aligned}
\vec{E}_a &= E_a\hat{\varepsilon}_0 \cos k_L x|\cos\omega t|e^{-i[\omega_a t + \eta(t)]},\\
\vec{E}_b &= E_b\hat{\varepsilon}_- e^{-i(k_L z + \omega_b t)},\\
\vec{E}_c &= E_c\hat{\varepsilon}_0 \cos k_L x|\cos\omega t|e^{-i\omega_c t},
\end{aligned} \tag{18}$$

where E_j and ω_j ($j = a, b, c$) are the amplitude and angular frequency of the electric field of each laser. $\hat{\varepsilon}_0$, $\hat{\varepsilon}_+$ and $\hat{\varepsilon}_-$ are π, σ^+ and σ^- polarization vectors, respectively. With the detailed calculation in Appendix C, the Raman coupling Hamiltonian can be constructed into the desired form, given by Eq. (2). Notice that in Eq. (18), the signum function in $\eta(t)$ adds an additional relative phase between laser a and b

changing between 0 and π periodically, and thus it ensures the $\cos \omega t$ driving pattern of the matrix element in the Raman coupling Hamiltonian. In our calculations, we apply $\hbar\omega = 20E_r$ with Raman laser wavelengths close to 791 and 806 nm (see Appendix C), which are achievable in the laboratory. With our laser configurations, the depth of the lattice potential induced by the AC Stark shift trapping effect of Raman lasers a and c is smaller than $0.15E_r$, which has a negligible influence on the momentum distribution of the quantum gas. These parameters result in a total laser power of around 0.8 W with Gaussian laser beams with beam waists of 200 μm, and a scattering limited lifetime of $\tau_{\mathrm{sc}} \approx 133$ ms, which is enough for experimental applications.

B. Loading the system and observation of the effects

To load the system into the ground state of the TMDOL, one can start from a cigar-shaped Bose–Einstein condensate with the desired atom number in an optical dipole trap with the long axis of the trap aligned with the x axis in the laboratory frame. Then the 2D optical lattice along the y and z axes should be turned on adiabatically to avoid excitation to higher bands of the optical lattice (e.g., $30E_r$ with $\lambda_\perp = 852$ nm for ^{87}Rb). Next, one can apply the shortcut adiabatic loading technique [51–54] to avoid excitations while loading the Bose gas into the ground state of a moving 2D optical lattice with an approximate wave function given by Eq. (10). Due to the relative motion between the lattice along the z axis and the laboratory frame, the atoms will carry a transverse momentum with expectation value $\langle p_z\rangle = -\hbar\bar{k}_z$ in the moving lattice frame. After setting the average transverse momentum, we can adiabatically turn on the Raman coupling Hamiltonian in Eq. (2), and the system will have been loaded into the ground state of the effective 1D optical lattice with a certain average transverse momentum, $\langle p_z\rangle$.

To observe the effect caused by the TMDOL in a Bose gas system, one can use time-of-flight (TOF) imaging. With our Floquet system, one can suddenly shut off all lasers at the end of the periodic driving cycle as the micromotion operator U becomes the identity operator so that the system is automatically projected from Floquet basis to the Zeeman sublevel basis [34]. Then, a TOF imaging can be performed with the imaging beam aligned along the z axis. The interference pattern contrast, $\mathcal{I}$ (visibility of the momentum peak along the x axis) can be measured from the TOF image [21,55], and $\mathcal{I}$ should change with $\langle p_z\rangle$ and the total number of atoms in the system, which sets the chemical potential. Thus we can observe the SF-MI phase transition as $\langle p_z\rangle$ changes.

V. CONCLUSION

We proposed an experimentally feasible method to create an effective 1D transverse-momentum-dependent optical lattice induced by an artificial gauge potential in a periodically driven system with Raman couplings. We constructed the single-particle effective Hamiltonian and investigated the many-body physics of the system with a non-negligible interaction by constructing the effective 1D Bose-Hubbard model with a deep 2D transverse confinement. Using the strong coupling expansion technique, we calculated the phase diagram of the effective 1D Bose-Hubbard model, and showed that the SF-MI transition can be tuned by changing the average transverse momentum $\langle p_z\rangle$ of the effective 1D Bose gas. We examined and confirmed our result using a QMC calculation with a continuous effective 1D lattice potential and found good agreement with the Bose-Hubbard model calculations. Then, we proposed a possible experimental implementation that achieves the desired periodically driven Hamiltonian and includes loading and measurement processes.

Our work provides a new platform for studying the many-body physics of a cold atom system with an artificial gauge potential. Specifically, in our TMDOL system, the phase of the quantum gas in the longitudinal direction is determined by the motional state in the transverse direction. With such a feature, the TMDOL makes it possible to create two spatially overlapping BECs of the same species in different phases, which gives rise to an interesting opportunity to study if the two BECs, one in SF and one in MI, will exchange their phases during a collision in which they exchange their momenta. Additionally, more complicated TMDOL potentials may be considered. One could change the transverse momentum distribution of the Bose gas by engineering the potential along the z axis to tune the transverse-momentum-dependent part of the potential, and a two-dimensional TMDOL could be achieved by introducing Raman lasers along both the x and y axes. One can also regard the transverse momentum in a TMDOL system as a continuous synthetic dimension, which is different from previous works on synthetic dimensions in Bose gases [24,28,56]. Also, another exciting future direction is considering both spin components in the TMDOL so that it becomes spin-dependent. By tuning the interaction between the spin components, the TMDOL can be an ideal platform to explore the phase diagram of the two-component Bose-Hubbard model. Finally, for fermionic systems, one could also implement a TMDOL with appropriate Raman couplings, and such a system provides a broad playground for studying transverse-momentum-dependent spin dynamics and many-body phases.

ACKNOWLEDGMENTS

We thank Thierry Giamarchi for insightful discussions. This work is supported by NSF grant PHY 1708008, NASA/JPL RSA 1656126, and the Swiss National Science Foundation under Division II. Numerical calculations make use of the ALPS scheduler library and statistical analysis tools [57–59].

APPENDIX A: ZEROTH-ORDER COMPONENT OF THE FLOQUET HAMILTONIAN AND ADIABATIC CONDITION

In this work, the system we consider satisfies the Floquet adiabatic condition given by Eq. (4). We can rewrite Eq. (3) in the form

$$H_F = \frac{\vec{p}^2}{2M} + \frac{1}{2M}(\vec{A}\cdot\vec{p} + \vec{p}\cdot\vec{A}) + \frac{\vec{A}^2}{2M} + V_{\mathrm{ext}}(\vec{r}). \quad \text{(A1)}$$

The adiabatic condition can be rewritten as

$$\left|\langle\vec{k}|\left[\frac{1}{2M}(\vec{A}\cdot\vec{p} + \vec{p}\cdot\vec{A}) + \frac{\vec{A}^2}{2M}\right]^{(n)}|\vec{k}'\rangle\right| \ll \hbar\omega(n \neq 0), \quad \text{(A2)}$$

where $[\cdots]^{(n)}$ is the nth Fourier component. From Eq. (A2), we can see that the adiabatic condition depends not only on the ratio Ω_0/ω, but also on the momentum of the particle. A rigorous solution of the adiabatic condition can be lengthy, so we focus on a operational condition.

We first work on the term $\vec{A}^2/2M$. Writing down the analytic form of the vector potential $\vec{A}$:

$$A_\xi = d_{1\xi} + d_{2\xi} + d_{3\xi}, \tag{A3}$$

where

$$\begin{aligned} d_{1\xi} &= \hbar a \sin\omega t \frac{(\vec{\Omega}\cdot\partial_\xi\vec{\Omega})(\vec{\Omega}\cdot\vec{\sigma})}{2|\Omega|^3}, \\ d_{2\xi} &= \hbar \sin(a\sin\omega t)\frac{[(\vec{\Omega}\times\partial_\xi\vec{\Omega})\times\vec{\Omega}]\cdot\vec{\sigma}}{2|\Omega|^3}, \\ d_{3\xi} &= \hbar[\cos(a\sin\omega t)-1]\frac{\vec{\Omega}\times\partial_\xi\vec{\Omega}\cdot\vec{\sigma}}{2|\Omega|^2}, \end{aligned} \tag{A4}$$

are the ξth component of vectors $\vec{d}_1$, $\vec{d}_2$, and $\vec{d}_3$. Then

$$\begin{aligned} A_\xi^2 = {} & d_{1\xi}^2 + d_{2\xi}^2 + d_{3\xi}^2 + (d_{1\xi}d_{2\xi} + d_{2\xi}d_{1\xi}) \\ & + (d_{1\xi}d_{3\xi} + d_{3\xi}d_{1\xi}) + (d_{2\xi}d_{3\xi} + d_{3\xi}d_{2\xi}). \end{aligned} \tag{A5}$$

We can simplify Eq. (A5) by noticing that the last three terms in the parenthesis vanish:

$$\begin{aligned} (d_{1\xi}d_{2\xi} + d_{2\xi}d_{1\xi}) &\propto \Omega_i\partial_\xi\Omega_i\Omega_j\hat{\sigma}_j\epsilon_{klm}C_{\xi k}\Omega_l\hat{\sigma}_m \\ &\quad + \epsilon_{klm}C_{\xi k}\Omega_l\hat{\sigma}_m\Omega_i\partial_\xi\Omega_i\Omega_j\hat{\sigma}_j \\ &= \Omega_i\partial_\xi\Omega_i\Omega_j\epsilon_{klm}C_{\xi k}\Omega_l(\hat{\sigma}_j\hat{\sigma}_m + \hat{\sigma}_m\hat{\sigma}_j) \\ &= 0, \\ (d_{2\xi}d_{3\xi} + d_{3\xi}d_{2\xi}) &\propto \epsilon_{ijk}C_{\xi i}\Omega_j\hat{\sigma}_k C_{\xi l}\hat{\sigma}_l \\ &\quad + C_{\xi l}\hat{\sigma}_l\epsilon_{ijk}C_{\xi i}\Omega_j\hat{\sigma}_k \\ &= \epsilon_{ijk}C_{\xi i}\Omega_j C_{\xi l}(\hat{\sigma}_k\hat{\sigma}_l + \hat{\sigma}_l\hat{\sigma}_k) \\ &= 0, \\ (d_{1\xi}d_{3\xi} + d_{3\xi}d_{1\xi}) &\propto \Omega_i\partial_\xi\Omega_i\Omega_j\hat{\sigma}_j C_{\xi k}\hat{\sigma}_k \\ &\quad + C_{\xi k}\hat{\sigma}_k\Omega_i\partial_\xi\Omega_i\Omega_j\hat{\sigma}_j \\ &= \Omega_i\partial_\xi\Omega_i\Omega_j C_{\xi k}(\hat{\sigma}_j\hat{\sigma}_k + \hat{\sigma}_k\hat{\sigma}_j) \\ &= 2\Omega_i\partial_\xi\Omega_i\Omega_j\epsilon_{jlm}\Omega_l\partial_\xi\Omega_m \\ &= 0, \end{aligned} \tag{A6}$$

where we let $C_{\xi i} = \{\vec{\Omega}\times\partial_\xi\vec{\Omega}\}_i = \epsilon_{ijk}\Omega_j\partial_\xi\Omega_k$ and we used the property $\hat{\sigma}_i\hat{\sigma}_j + \hat{\sigma}_j\hat{\sigma}_i = 2\delta_{ij}$.

After the simplification above, Eq. (A5) becomes

$$\begin{aligned} A_\xi^2 = {} & \hbar^2 a^2 \sin^2\omega t \frac{(\vec{\Omega}\cdot\partial_\xi\vec{\Omega})^2}{4|\Omega|^4} \\ & + 2\hbar^2[1-\cos(a\sin\omega t)]\frac{|\Omega|^2(\partial_\xi\vec{\Omega})^2 - (\vec{\Omega}\cdot\partial_\xi\vec{\Omega})^2}{4|\Omega|^4}. \end{aligned} \tag{A7}$$

We can expand $\cos(a\sin\omega t)$ into an expansion of Bessel functions of the first kind as

$$\cos(a\sin\omega t) = J_0(a) + 2\sum_{m=1}^{\infty} J_{2m}(a)\cos(2m\omega t), \tag{A8}$$

the zeroth-order Fourier term of $\vec{A}^2/2M$ is

$$\left[\frac{\vec{A}^2}{2M}\right]^{(0)} = \left\{\frac{1}{16}a_0^2(1-\cos 2k_Lx) + \frac{1}{2}[1-J_0(a)]\right\}E_r, \tag{A9}$$

and the second order (±2) harmonic terms are

$$\left[\frac{\vec{A}^2}{2M}\right]^{(\pm 2)} = \left[\frac{1}{32}a_0^2\cos 2k_Lx \pm \frac{i}{2}J_2(a)\right]E_r. \tag{A10}$$

Next, we calculate the contribution of the $\frac{1}{2M}(\vec{A}\cdot\vec{p} + \vec{p}\cdot\vec{A})$ term. From Eq. (A4), we get

$$\begin{aligned} \vec{A} = {} & \tfrac{1}{2}\hbar k_L\{[-a_0\sin k_Lxe^{-ik_Lz}\sin\omega t\hat{x} \\ & + ie^{ik_Lz}\sin(a\sin\omega t)\mathrm{sgn}(a)\hat{z}]\hat{\sigma}_+ + \mathrm{H.c.}\} \\ & + \tfrac{1}{2}\hbar k_L[\cos(a\sin\omega t)-1]\hat{\sigma}_3\hat{z}, \end{aligned} \tag{A11}$$

where $\mathrm{sgn}(\cdot)$ is the signum function, $\hat{\sigma}_+ = (\hat{\sigma}_1 - i\hat{\sigma}_2)/\sqrt{2}$, and $\hat{x}$ and $\hat{z}$ are unit vectors along the x and z axes. Then, we can write down the absolute value of the nonzero matrix element of the Floquet Hamiltonian that is proportional to the first Fourier order,

$$\begin{aligned} & \langle k_x, k_z, \uparrow|H_F^{(\pm 1)}|k_x', k_z', \downarrow\rangle \\ & = \pm\frac{a_0}{8}E_r\left\{\langle k_x, k_z, \uparrow|\left[(e^{ik_Lx} - e^{-ik_Lx})e^{-ik_Lz}\frac{k_x'}{k_L}\right]|k_x', k_z', \downarrow\rangle\right. \\ & \quad \left. + \langle k_x, k_z, \uparrow|\left[\frac{k_x}{k_L}(e^{ik_Lx} - e^{-ik_Lx})e^{ik_Lz}\right]|k_x', k_z', \downarrow\rangle\right\} \\ & \quad \pm\frac{E_r}{2}\langle k_x, k_z, \uparrow|J_1(a)\mathrm{sgn}(a)\left(e^{ik_Lz}\frac{k_z}{k_L}\right. \\ & \quad \left.\mp e^{-ik_Lz}\frac{k_z'}{k_L}\right)|k_x', k_z', \downarrow\rangle, \end{aligned}$$

where $|\uparrow (\downarrow)\rangle$ indicates two spin states. Notice that the above equation can be split into several matrix elements between different momentum states. After collecting terms and simplifying, we get the adiabatic condition for the first Fourier order as

$$\begin{aligned} & \left\{\frac{a_0}{8}\left|\frac{k_x}{k_L}\right| + \frac{1}{2}|\langle k_L|\mathrm{sgn}(a)J_1(a)|k_L \pm 1\rangle|\left|\frac{k_z}{k_L}\right|\right\}E_r \\ & = \frac{1}{2}\left\{\left|\frac{k_x}{k_L}\right| + 0.19\left|\frac{k_z}{k_L}\right|\right\}E_r \ll \hbar\omega, \end{aligned} \tag{A12}$$

where we evaluated $|\langle k_L|\mathrm{sgn}(a)J_1(a)|k_L \pm 1\rangle|$ numerically to be 0.19 by setting $a_0 = 4$. In our calculations, we use $\hbar\omega/E_r = 20$, and we can get the adiabatic condition for the first Fourier order by combining the two conditions in Eq. (A12) to be $|k_x/k_L| + 0.19|k_z/k_L| \ll 40$. We also evaluate the matrix elements between higher order momentum states, and find that they are much smaller than the matrix element in Eq. (A12).

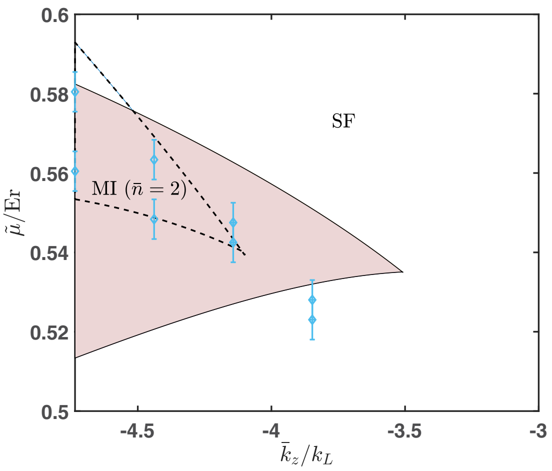

FIG. 5. $\bar{n} = 2$ Mott lobe. The pink shaded area with black solid line boundaries is calculated from the occupation-independent Bose-Hubbard model, blue diamonds with error bars ($\pm 0.005Er$) are QMC calculation results, and black dashed lines are Bose-Hubbard model calculation results with a band mixing ground state $|\psi_g\rangle \approx 0.994|s\rangle + 0.109|d\rangle$.

Next, we consider the second order Fourier components. Both $\frac{1}{2M}(\vec{A}\cdot\vec{p} + \vec{p}\cdot\vec{A})$ and the A^2 term contribute to the even order $\sin 2m\omega t$ terms. Specifically for the second order, from Eqs. (A10) and (A11), we can get the matrix element of second Fourier component.

$$\begin{aligned}
&\langle k_x, k_z, \uparrow(\downarrow)|H_F^{(\pm 2)}|k_x', k_z, \uparrow(\downarrow)\rangle \\
&\quad = \langle k_x, k_z, \uparrow(\downarrow)|\left[\frac{1}{64}a_0^2 \pm \frac{i}{2}J_2(a)\right]E_r|k_x' \pm 2k_L, k_z, \uparrow(\downarrow)\rangle \\
&\qquad + \langle k_x, k_z, \uparrow(\downarrow)|2\frac{k_z}{k_L}J_2(a)E_r|k_x' \pm 2k_L, k_z, \uparrow(\downarrow)\rangle \\
&\quad \approx \left(\frac{1}{64}a_0^2 \pm 0.1i - 0.4\frac{k_z}{k_L}\right)E_r\delta(k_x - k_x' \pm 2k_L), \qquad \text{(A13)}
\end{aligned}$$

where we used $\langle k_x|J_2(a)|k_x \pm 2k_L\rangle = -0.20$ from numerical evaluation by setting $a_0 = 4$, and the adiabatic condition for the second Fourier order becomes $|(\frac{1}{64}a_0^2 \pm 0.1i - 0.4\frac{k_z}{k_L})E_r| \ll \hbar\omega$. By setting $\hbar\omega/E_r = 20$, we get $|k_z/k_L| \ll 49$. Combining this result with $|k_x/k_L| + 0.19|k_z/k_L| \ll 40$ yields $|k_x/k_L| \ll 31$ For higher order Fourier terms, one can calculate and see that the adiabatic conditions are all weaker than the first two Fourier terms. In our calculations, the above adiabatic conditions, $|k_x/k_L| \ll 31$ and $|k_z/k_L| \ll 49$, can easily be satisfied.

APPENDIX B: PHASE DIAGRAM AROUND $\bar{n} = 2$ MOTT LOBE

In Sec. III, we showed the phase diagram of our effective 1D optical lattice and found good agreement between our effective 1D Bose-Hubbard model and QMC calculations on the $\bar{n} = 1$ Mott lobe. Here, we show the $\bar{n} = 2$ Mott lobe in Fig. 5. There is a significant difference between the Bose-Hubbard model (pink shaded area with black solid line boundaries) and the QMC calculations (blue diamonds with error bars). We believe that the disagreement is caused by the occupation-dependence of the tunneling and interactions terms, which is not captured by the occupation-independent Bose-Hubbard model. Our QMC calculation is more accurate because we used a continuous potential in the QMC calculations instead of the Bose-Hubbard model. In previous works, occupation-dependent tunneling and onsite interactions in a modified Bose-Hubbard model have been explored [47–49], and the true many-body ground state was found to be a band mixing state. In our calculations, we phenomenologically find a mixing state with $|\psi_g\rangle \approx 0.994|s\rangle + 0.109|d\rangle$, where $|s\rangle$ and $|d\rangle$ are the single-particle eigenstates of the s and d-bands, respectively. By treating the degree of mixing as an adjustable parameter, we found that the modified Bose-Hubbard results (black dashed lines) have better agreement with the QMC calculations. This agrees with the finding in Ref. [47] that the population on higher orbitals was less than 1%. Although for more rigorous analysis one needs to numerically diagonalize the many-body Hamiltonian [47–49], we believe that our qualitative calculations are sufficient to indicate that band mixing is the source of the disagreement between the Bose-Hubbard and QMC $\bar{n} = 2$ Mott lobe. Also, we want to point out that the band mixing effect mentioned here is a general effect in all optical lattice potentials with sufficiently strong interactions, and is not a unique feature of the TMDOL.

APPENDIX C: DETAILED CONSTRUCTION OF THE EFFECTIVE TWO-LEVEL MULTILASER RAMAN PROCESS AND LIFETIME ESTIMATION

Using second order perturbation theory, we can calculate the effective Hamiltonian of the ground state manifold of the atom from the multilaser Raman process Hamiltonian [50,60]. Here, we consider the ^{87}Rb atom $|5S_{\frac{1}{2}}, F = 1\rangle$ manifold to be our system. More specifically, we consider $|1\rangle = |F = 1, m_F = -1\rangle$, $|2\rangle = |F = 1, m_F = 0\rangle$ and $|3\rangle = |F = 1, m_F = 1\rangle$. By applying a bias magnetic field $\vec{B}$, we can define the $+z$ direction and then we choose our Raman laser a to be a standing wave along the x axis with π polarization, laser b to propagate along the $+z$ direction with σ^- polarization, and laser c to be a standing wave along the x axis with π polarization with the opposite detuning as laser a to cancel the spatially dependent AC stark shift. Specifically, lasers a and b are blue detuned from the ^{87}Rb D_1 transition and laser c is red detuned from the D_1 transition. All the wavelengths of the Raman lasers can be achieved in the laboratory (e.g., with Ti:Sapphire lasers). All one-photon detunings are much larger than the Rabi frequencies so that there is negligible transitions to excited states. The level diagram is shown in Fig. 4. We only consider the D_1 and D_2 lines, as all other atomic states are too far from the laser frequencies we consider to have appreciable coupling.

Similar to the calculations in previous works [34,50], we can write the reduced three-level effective Hamiltonian for the

Raman process with the laser fields in Eq. (18)

$$H_R = \sum_{\mathcal{D},F'} \sum_{m_F=-1}^{1} \left\{ \left[\frac{\left(c_{\mathcal{D},F,F'}^{m_F,m_F}\right)^2}{\Delta_{a,F,F',\mathcal{D}}^{m_F,m_F}} |\Omega_{a,\mathcal{D}}|^2 + \frac{\left(c_{\mathcal{D},F,F'}^{m_F-1,m_F}\right)^2}{\Delta_{b,F,F',\mathcal{D}}^{m_F,m_F}} |\Omega_{b,\mathcal{D}}|^2 \right.\right.$$
$$\left. + \frac{\left(c_{\mathcal{D},F,F'}^{m_F,m_F}\right)^2}{\Delta_{c,F,F',\mathcal{D}}^{m_F,m_F}} |\Omega_{c,\mathcal{D}}|^2 + \delta_{m_F} \right] |m_F\rangle\langle m_F|$$
$$+ \frac{1}{2}\left(\frac{1}{\Delta_{a,F,F',\mathcal{D}}^{m_F,m_F}} + \frac{1}{\Delta_{b,F,F',\mathcal{D}}^{m_F+1,m_F}} \right) c_{\mathcal{D},F,F'}^{m_F,m_F} c_{\mathcal{D},F,F'}^{m_F-1,m_F}$$
$$\left. \times \Omega_{a,\mathcal{D}}^{*} \Omega_{b,\mathcal{D}} |m_F\rangle\langle m_F+1| + \text{H.c.} \right\}, \tag{C1}$$

where $F = 1$, $\mathcal{D} = 1, 2$ indicates the transitions for the D_1 and D_2 lines, $F' = 1, 2$ and $F' = 0, 1, 2$ for $\mathcal{D} = 1$ and $\mathcal{D} = 2$, respectively. $c_{\mathcal{D},F,F'}^{m_F,m_{F'}}$ is the Clebsh-Gordon coefficient between $|F, m_F\rangle$ and $|F', m_{F'}\rangle$ states for the D_1 (D_2) line, and $\Delta_{\zeta,F,F',\mathcal{D}}^{m_F,m_{F'}} = \omega_\zeta - (\omega_{F',m_{F'}}^{e} - \omega_{F,m_F}^{g})$ ($\zeta = a, b, c$) is the one-photon detuning, where ω_ζ, ω_{F,m_F}^{g}, and $\omega_{F',m_{F'}}^{e}$ are angular frequencies for laser $\zeta = a, b, c$ and the corresponding energy levels of the ground and excited state, respectively. $\Omega_{\zeta,\mathcal{D}} = -\vec{d}_{\mathcal{D}} \cdot \vec{E}_\zeta/\hbar$ ($\zeta = a, b, c$) are the Rabi frequencies, where $\vec{d}_{\mathcal{D}}$ ($\mathcal{D} = 1, 2$) are the effective dipole moment vectors of the D_1 and D_2 transitions, respectively. $|m_F\rangle = |F = 1, m_F = -1, 0, 1\rangle$ correspond to $|1\rangle$, $|2\rangle$, and $|3\rangle$, respectively. δ_{m_F} ($m_F = -1, 0, 1$) are defined as $\delta_{-1} = 0$, $\delta_0 = \Delta_{a,F,F',\mathcal{D}}^{-1,-1} - \Delta_{b,F,F',\mathcal{D}}^{-1,0}$ and $\delta_1 = \Delta_{a,F,F',\mathcal{D}}^{-1,-1} - \Delta_{b,F,F',\mathcal{D}}^{-1,0} + \Delta_{a,F,F',\mathcal{D}}^{0,0} - \Delta_{b,F,F',\mathcal{D}}^{0,1}$. Since lasers a and b are blue detuned from the D_1 line while laser c is red detuned, laser c only contributes to the AC stark shift terms in the diagonal matrix elements. If we rewrite Eq. (C1) as

$$H_R = H_{11}|1\rangle\langle 1| + H_{22}|2\rangle\langle 2| + H_{33}|3\rangle\langle 3|$$
$$+ H_{12}|1\rangle\langle 2| + H_{23}|2\rangle\langle 3| + \text{H.c.},$$

and if $H_{22} = H_{11}$ and $|H_{33} - H_{22}| \gg H_{23}$, then $|1\rangle$ and $|2\rangle$ are well isolated from the third state, $|3\rangle$, and the effective two-level Hamiltonian takes the form $H_e = H_{11}|1\rangle\langle 1| + H_{22}|2\rangle\langle 2| + H_{12}|1\rangle\langle 2| + \text{H.c.}$ The above condition can be satisfied by introducing proper laser frequencies in our Raman process. Specifically, in our calculations, with $a_0 = 4$, one group of possible experimental parameters are $B = 10$G, $\lambda_a \approx 791.56$ nm, $\lambda_b \approx 791.56$ nm, and $\lambda_c \approx 805.96$ nm. The two-photon detuning of the transition between $|1\rangle$ and $|2\rangle$ is around 400 kHz. All the time-dependent and spatially dependent AC Stark shifts in the diagonal elements are negligibly small due to the opposite AC stark shift caused by laser c. In fact, after cancellation, the depth of the lattice potential caused by the AC Stark shift of Raman lasers is smaller than $0.15E_r$, which is negligibly small. The corresponding Floquet driving frequency is $\omega = 2\pi \times 72$ kHz and $\Omega_0 = 2\pi \times 288$ kHz. The Raman laser intensities are $I_a \approx 24.2\text{W/cm}^2$, $I_b \approx 605\ \text{W/cm}^2$, and $I_d \approx 9.8\ \text{W/cm}^2$. Ignoring the constant term proportional to the identity matrix, we get the desired Hamiltonian H_d in Eq. (2) from the effective two-level Hamiltonian H_e.

The next issue we care about is the scattering limited lifetime of the Bose gas. Using the well-developed theory in optical scattering in cold atom ensemble [61], the scattering rate can be written as

$$\gamma_{\text{sc}} \approx \frac{\pi c^2 \Gamma^2}{2\hbar\omega_0^3}\left(\frac{2}{\Delta_{D_2}} + \frac{1}{\Delta_{D_1}}\right)(I_a + I_b + I_c), \tag{C2}$$

where c is the speed of light, $\Gamma \approx 2\pi \times 6$ MHz is the natural linewidth, Δ_{D_1} and Δ_{D_2} are one-photon detunings with respect to the D_1 and D_2 lines, respectively. By plugging in our parameters and using a Gaussian beam waist of 200 μm, the lifetime is $\tau_{\text{sc}} = 1/\gamma_{\text{sc}} \approx 133$ ms, which is sufficient for experimental applications.

---

[1] S. Sugawa, F. Salces-Carcoba, A. R. Perry, Y. Yue, and I. Spielman, Second chern number of a quantum-simulated non-Abelian yang monopole, Science **360**, 1429 (2018).

[2] S.-L. Zhu, H. Fu, C.-J. Wu, S.-C. Zhang, and L.-M. Duan, Spin Hall Effects for Cold Atoms in a Light-Induced Gauge Potential, Phys. Rev. Lett. **97**, 240401 (2006).

[3] X.-J. Liu, X. Liu, L. C. Kwek, and C. H. Oh, Optically Induced Spin-Hall Effect in Atoms, Phys. Rev. Lett. **98**, 026602 (2007).

[4] L. J. LeBlanc, K. Jiménez-García, R. A. Williams, M. C. Beeler, A. R. Perry, W. D. Phillips, and I. B. Spielman, Observation of a superfluid hall effect, Proc. Natl. Acad. Sci. USA **109**, 10811 (2012).

[5] M. C. Beeler, R. A. Williams, K. Jimenez-Garcia, L. J. LeBlanc, A. R. Perry, and I. B. Spielman, The spin hall effect in a quantum gas, Nature (London) **498**, 201 (2013).

[6] J. Dalibard, F. Gerbier, G. Juzeliūnas, and P. Öhberg, Colloquium: Artificial gauge potentials for neutral atoms, Rev. Mod. Phys. **83**, 1523 (2011).

[7] N. Goldman, G. Juzeliūnas, P. Öhberg, and I. B. Spielman, Light-induced gauge fields for ultracold atoms, Rep. Prog. Phys. **77**, 126401 (2014).

[8] H. Zhai, Degenerate quantum gases with spin–orbit coupling: a review, Rep. Prog. Phys. **78**, 026001 (2015).

[9] L. Zhang and X.-J. Liu, Spin-orbit coupling and topological phases for ultracold atoms, in *Synthetic Spin-Orbit Coupling in Cold Atoms* (World Scientific, Singapore, 2018), pp. 1–87.

[10] L. Huang, Z. Meng, P. Wang, P. Peng, S.-L. Zhang, L. Chen, D. Li, Q. Zhou, and J. Zhang, Experimental realization of two-dimensional synthetic spin–orbit coupling in ultracold fermi gases, Nat. Phys. **12**, 540 (2016).

[11] C. Hamner, Y. Zhang, M. Khamehchi, M. J. Davis, and P. Engels, Spin-Orbit-Coupled Bose-Einstein Condensates in a One-Dimensional Optical Lattice, Phys. Rev. Lett. **114**, 070401 (2015).

[12] Y.-J. Lin, K. Jiménez-García, and I. B. Spielman, Spin–orbit-coupled bose–einstein condensates, Nature (London) **471**, 83 (2011).

[13] X.-J. Liu, Z.-X. Liu, and M. Cheng, Manipulating Topological Edge Spins in a One-Dimensional Optical Lattice, Phys. Rev. Lett. **110**, 076401 (2013).

[14] Z. Wu, L. Zhang, W. Sun, X.-T. Xu, B.-Z. Wang, S.-C. Ji, Y. Deng, S. Chen, X.-J. Liu, and J.-W. Pan, Realization of

two-dimensional spin-orbit coupling for bose-einstein condensates, Science **354**, 83 (2016).

[15] Z.-Y. Wang, X.-C. Cheng, B.-Z. Wang, J.-Y. Zhang, Y.-H. Lu, C.-R. Yi, S. Niu, Y. Deng, X.-J. Liu, S. Chen *et al.*, Realization of an ideal weyl semimetal band in a quantum gas with 3d spin-orbit coupling, Science **372**, 271 (2021).

[16] I. Bloch, J. Dalibard, and W. Zwerger, Many-body physics with ultracold gases, Rev. Mod. Phys. **80**, 885 (2008).

[17] D. Jaksch, C. Bruder, J. I. Cirac, C. W. Gardiner, and P. Zoller, Cold Bosonic Atoms in Optical Lattices, Phys. Rev. Lett. **81**, 3108 (1998).

[18] G. Boéris, L. Gori, M. D. Hoogerland, A. Kumar, E. Lucioni, L. Tanzi, M. Inguscio, T. Giamarchi, C. D'Errico, G. Carleo, G. Modugno, and L. Sanchez-Palencia, Mott transition for strongly interacting one-dimensional bosons in a shallow periodic potential, Phys. Rev. A **93**, 011601(R) (2016).

[19] M. Greiner, O. Mandel, T. Esslinger, T. W. Hänsch, and I. Bloch, Quantum phase transition from a superfluid to a mott insulator in a gas of ultracold atoms, Nature (London) **415**, 39 (2002).

[20] E. Haller, R. Hart, M. J. Mark, J. G. Danzl, L. Reichsöllner, M. Gustavsson, M. Dalmonte, G. Pupillo, and H.-C. Nägerl, Pinning quantum phase transition for a Luttinger liquid of strongly interacting bosons, Nature (London) **466**, 597 (2010).

[21] P. Soltan-Panahi, J. Struck, P. Hauke, A. Bick, W. Plenkers, G. Meineke, C. Becker, P. Windpassinger, M. Lewenstein, and K. Sengstock, Multi-component quantum gases in spin-dependent hexagonal lattices, Nat. Phys. **7**, 434 (2011).

[22] J. Struck, C. Ölschläger, M. Weinberg, P. Hauke, J. Simonet, A. Eckardt, M. Lewenstein, K. Sengstock, and P. Windpassinger, Tunable Gauge Potential for Neutral and Spinless Particles in Driven Optical Lattices, Phys. Rev. Lett. **108**, 225304 (2012).

[23] M. Aidelsburger, M. Atala, M. Lohse, J. T. Barreiro, B. Paredes, and I. Bloch, Realization of the Hofstadter Hamiltonian with Ultracold Atoms in Optical Lattices, Phys. Rev. Lett. **111**, 185301 (2013).

[24] A. Celi, P. Massignan, J. Ruseckas, N. Goldman, I. B. Spielman, G. Juzeliūnas, and M. Lewenstein, Synthetic Gauge Fields in Synthetic Dimensions, Phys. Rev. Lett. **112**, 043001 (2014).

[25] F. A. An, E. J. Meier, and B. Gadway, Engineering a Flux-Dependent Mobility Edge in Disordered Zigzag Chains, Phys. Rev. X **8**, 031045 (2018).

[26] Z. Cai, X. Zhou, and C. Wu, Magnetic phases of bosons with synthetic spin-orbit coupling in optical lattices, Phys. Rev. A **85**, 061605 (2012).

[27] W. S. Cole, S. Zhang, A. Paramekanti, and N. Trivedi, Bose-Hubbard Models with Synthetic Spin-Orbit Coupling: Mott Insulators, Spin Textures, and Superfluidity, Phys. Rev. Lett. **109**, 085302 (2012).

[28] B. Gadway, Atom-optics approach to studying transport phenomena, Phys. Rev. A **92**, 043606 (2015).

[29] E. J. Meier, F. A. An, and B. Gadway, Atom-optics simulator of lattice transport phenomena, Phys. Rev. A **93**, 051602 (2016).

[30] F. A. An, E. J. Meier, B. Gadway *et al.*, Correlated Dynamics in a Synthetic Lattice of Momentum States, Phys. Rev. Lett. **120**, 040407 (2018).

[31] F. A. An, B. Sundar, J. Hou, X.-W. Luo, E. J. Meier, C. Zhang, K. R. Hazzard, and B. Gadway, Nonlinear Dynamics in a Synthetic Momentum-State Lattice, Phys. Rev. Lett. **127**, 130401 (2021).

[32] P. Račkauskas, V. Novičenko, H. Pu, and G. Juzeliūnas, Non-Abelian geometric potentials and spin-orbit coupling for periodically driven systems, Phys. Rev. A **100**, 063616 (2019).

[33] V. Novičenko and G. Juzeliūnas, Non-abelian geometric phases in periodically driven systems, Phys. Rev. A **100**, 012127 (2019).

[34] Z. Chen, J. D. Murphree, and N. P. Bigelow, Su (2) geometric phase induced by a periodically driven raman process in an ultracold dilute bose gas, Phys. Rev. A **101**, 013606 (2020).

[35] T. Stöferle, H. Moritz, C. Schori, M. Köhl, and T. Esslinger, Transition from a Strongly Interacting 1D Superfluid to a Mott Insulator, Phys. Rev. Lett. **92**, 130403 (2004).

[36] E. Anisimovas, M. Račiūnas, C. Sträter, A. Eckardt, I. Spielman, and G. Juzeliūnas, Semisynthetic zigzag optical lattice for ultracold bosons, Phys. Rev. A **94**, 063632 (2016).

[37] L. Barbiero and L. Salasnich, Quantum bright solitons in a quasi-one-dimensional optical lattice, Phys. Rev. A **89**, 063605 (2014).

[38] T. D. Kühner and H. Monien, Phases of the one-dimensional bose-hubbard model, Phys. Rev. B **58**, R14741 (1998).

[39] S. Ejima, H. Fehske, F. Gebhard, K. zu Münster, M. Knap, E. Arrigoni, and W. von der Linden, Characterization of mott-insulating and superfluid phases in the one-dimensional bose-hubbard model, Phys. Rev. A **85**, 053644 (2012).

[40] T. Wang, X.-F. Zhang, C.-F. Hou, S. Eggert, A. Pelster *et al.*, High-order symbolic strong-coupling expansion for the bose-hubbard model, Phys. Rev. B **98**, 245107 (2018).

[41] D. M. Ceperley, Path integrals in the theory of condensed helium, Rev. Mod. Phys. **67**, 279 (1995).

[42] M. Boninsegni, N. Prokof'ev, and B. Svistunov, Worm Algorithm for Continuous-Space Path Integral Monte Carlo Simulations, Phys. Rev. Lett. **96**, 070601 (2006).

[43] M. Boninsegni, N. V. Prokof'ev, and B. V. Svistunov, Worm algorithm and diagrammatic Monte Carlo: A new approach to continuous-space path integral Monte Carlo simulations, Phys. Rev. E **74**, 036701 (2006).

[44] H. Yao, D. Clément, A. Minguzzi, P. Vignolo, and L. Sanchez-Palencia, Tan's Contact for Trapped Lieb-Liniger Bosons at Finite Temperature, Phys. Rev. Lett. **121**, 220402 (2018).

[45] H. Yao, T. Giamarchi, and L. Sanchez-Palencia, Lieb-Liniger Bosons in a Shallow Quasiperiodic Potential: Bose Glass Phase and Fractal Mott Lobes, Phys. Rev. Lett. **125**, 060401 (2020).

[46] R. Gautier, H. Yao, and L. Sanchez-Palencia, Strongly Interacting Bosons in a Two-Dimensional Quasicrystal Lattice, Phys. Rev. Lett. **126**, 110401 (2021).

[47] D.-S. Lühmann, O. Jürgensen, and K. Sengstock, Multi-orbital and density-induced tunneling of bosons in optical lattices, New J. Phys. **14**, 033021 (2012).

[48] O. Dutta, A. Eckardt, P. Hauke, B. Malomed, and M. Lewenstein, Bose–hubbard model with occupation-dependent parameters, New J. Phys. **13**, 023019 (2011).

[49] U. Bissbort, F. Deuretzbacher, and W. Hofstetter, Effective multibody-induced tunneling and interactions in the bose-hubbard model of the lowest dressed band of an optical lattice, Phys. Rev. A **86**, 023617 (2012).

[50] K. Wright, L. Leslie, and N. Bigelow, Raman coupling of zeeman sublevels in an alkali-metal bose-einstein condensate, Phys. Rev. A **78**, 053412 (2008).

[51] E. Torrontegui, S. Ibáñez, X. Chen, A. Ruschhaupt, D. Guéry-Odelin, and J. Muga, Fast atomic transport without vibrational heating, Phys. Rev. A **83**, 013415 (2011).

[52] R. Corgier, S. Amri, W. Herr, H. Ahlers, J. Rudolph, D. Guéry-Odelin, E. M. Rasel, E. Charron, and N. Gaaloul, Fast manipulation of bose–einstein condensates with an atom chip, New J. Phys. **20**, 055002 (2018).

[53] D. Guéry-Odelin, A. Ruschhaupt, A. Kiely, E. Torrontegui, S. Martínez-Garaot, and J. G. Muga, Shortcuts to adiabaticity: Concepts, methods, and applications, Rev. Mod. Phys. **91**, 045001 (2019).

[54] Y. Ding, T.-Y. Huang, K. Paul, M. Hao, and X. Chen, Smooth bang-bang shortcuts to adiabaticity for atomic transport in a moving harmonic trap, Phys. Rev. A **101**, 063410 (2020).

[55] F. Gerbier, A. Widera, S. Fölling, O. Mandel, T. Gericke, and I. Bloch, Interference pattern and visibility of a mott insulator, Phys. Rev. A **72**, 053606 (2005).

[56] H. M. Price, T. Ozawa, and N. Goldman, Synthetic dimensions for cold atoms from shaking a harmonic trap, Phys. Rev. A **95**, 023607 (2017).

[57] M. Troyer, B. Ammon, and E. Heeb, Parallel object oriented Monte Carlo simulations, Lect. Notes Comput. Sci. **1505**, 191 (1998).

[58] A. Albuquerque, F. Alet, P. Corboz, P. Dayal, A. Feiguin, S. Fuchs, L. Gamper, E. Gull, S. Guertler, A. Honecker, R. Igarashi, M. Koerner, A. Kozhevnikov, A. Laeuchli, S. Manmana, M. Matsumoto, I. McCulloch, F. Michel, R. Noack, G. Pawlowski, L. Pollet, T. Pruschke, U. Schollwöck, S. Todo, S. Trebst, M. Troyer, P. Werner, and S. Wessel, The ALPS project release 1.3: Open-source software for strongly correlated systems, J. Magn. Magn. Mater. **310**, 1187 (2007).

[59] B. Bauer, L. D. Carr, H. G. Evertz, A. Feiguin, J. Freire, S. Fuchs, L. Gamper, J. Gukelberger, E. Gull, S. Guertler *et al.*, The ALPS project release 2.0: Open source software for strongly correlated systems, J. Stat. Mech. (2011) P05001.

[60] C. Cohen-Tannoudji, J. Dupont-Roc, and G. Grynberg, *Atom-Photon Interactions: Basic Processes and Applications* (Wiley-VCH, Germany, 1998).

[61] R. Grimm, M. Weidemüller, and Y. B. Ovchinnikov, Optical dipole traps for neutral atoms, Adv. At. Mol. Opt. Phys. **42**, 95 (2000).